OPEN ACCESS



Bursts from High-magnetic-field Pulsars Swift J1818.0-1607 and PSR J1846.4-0258

Mete Uzuner b, Özge Keskin b, Yuki Kaneko b, Ersin Göğüş b, Oliver J. Roberts b, Lin Lin b, Matthew G. Baring b, Can Güngör b, Chryssa Kouveliotou b, Alexander J. van der Horst b, and George Younes b, and George Younes b, and George Younes b, Sabancı University, Faculty of Engineering and Natural Sciences, İstanbul 34956 Turkey; meteuzuner sabancı inviv. edu Science and Technology Institute, Universities Space and Research Association, 320 Sparkman Drive, Huntsville, AL 35805, USA.

3 Department of Astronomy, Beijing Normal University, Beijing 100875, People's Republic of China Popartment of Physics and Astronomy—MS 108, Rice University, 6100 Main Street, Houston, TX 77251-1892, USA Sistanbul University, Science Faculty, Department of Astronomy and Space Sciences, Beyazt, İstanbul 34119 Turkey Department of Physics, The George Washington University, 725 21st Street NW, Washington, DC 20052, USA

Astronomy, Physics, and Statistics Institute of Sciences (APSIS), The George Washington University, Washington, DC 20052, USA

Astrophysics Science Division, NASA/GSFC, Greenbelt, MD 20771, USA

Received 2022 August 29; revised 2022 November 2; accepted 2022 November 19; published 2022 December 28

Abstract

The detection of magnetar-like bursts from highly magnetic ($B > 10^{13}$ G) rotation-powered pulsars (RPPs) opened the magnetar population to yet another group of neutron stars. At the same time the question arose as to whether magnetar-like bursts from high-B RPPs have similar characteristics to bursts from known magnetar sources. We present here our analyses of the Fermi Gamma-ray Burst Monitor (GBM) data from two magnetar candidates, Swift J1818.0–1607 (a radio-loud magnetar) and PSR J1846.4–0258. Both sources entered active bursting episodes in 2020 triggering Fermi-GBM in 2020 and in early 2021. We searched for untriggered bursts from both sources and performed temporal and spectral analyses on all events. Here, we present the results of our comprehensive burst search and analyses. We identified 37 and 58 bursts that likely originated from Swift J1818.0 – 1607 and PSR J1846.4–0258, respectively. We find that the bursts from these sources are shorter on average than typical magnetar bursts. In addition, their spectra are best described with a single blackbody function with $kT \sim 10$ –11 keV; several relatively bright events, however, show higher energy emission that could be modeled with a cutoff power-law model. We find that the correlation between the blackbody emitting area and the spectral temperature for the burst ensemble of each pulsar deviates from the ideal Stefan–Boltzmann law, as it does for some burst-active magnetars. We interpret this characteristic as being due to the significant radiation anisotropy expected from optically thick plasmas in very strong magnetic fields.

Unified Astronomy Thesaurus concepts: Magnetars (992); X-ray bursts (1814); Neutron stars (1108); Rotation powered pulsars (1408)

1. Introduction

Magnetars are young neutron stars with extreme magnetic field strengths, 10^{14} – 10^{15} G (Duncan & Thompson 1992; Kouveliotou et al. 1998). Such immense fields interacting with the highly condensed material of those compact bodies yield a variety of observable phenomena, such as energetic bursts, pulsed persistent emission, etc. (Thompson & Duncan 1995, 1996) detected in nearly all parts of the electromagnetic spectrum (see Kaspi & Beloborodov 2017 for a review). The most common characteristic of magnetar activities is the repeated emission of short duration, highly energetic hard X-ray bursts with luminosities exceeding the Eddington limit (Gogus et al. 1999, 2000; van der Horst et al. 2012; Lin et al. 2020a; Younes et al. 2021). Recent observations of an energetic X-ray burst from a Galactic magnetar, SGR J1935+2154 (e.g., Mereghetti et al. 2020), coincident with a bright fast radio burst (Bochenek et al. 2020; CHIME/FRB Collaboration 2020), demonstrated that magnetars could indeed be responsible for some enigmatic FRBs originating from distant galaxies (see Petroff et al. 2019, 2021 for a review of FRBs).

Typical magnetar bursts are short, usually lasting about $0.1\,\mathrm{s}$ with peak luminosities reaching $10^{41}\,\mathrm{erg\,s^{-1}}$. Their spectral

Original content from this work may be used under the terms of the Creative Commons Attribution 4.0 licence. Any further distribution of this work must maintain attribution to the author(s) and the title of the work, journal citation and DOI.

energy distributions in hard X-rays are well described using either a power-law function with exponential cutoff or a double-blackbody function (Gogus et al. 1999, 2000; Israel et al. 2008; Lin et al. 2012; van der Horst et al. 2012; von Kienlin et al. 2012; Younes et al. 2014; Lin et al. 2020a, 2020b). These events are generally attributed to crustal deformations at local sites of magnetars as a result of strong magnetic pressure build up (Thompson & Duncan 1995; Gourgouliatos & Lander 2021). Additionally, magnetospheric reconnection processes are also considered to possibly account for these events (Thompson & Duncan 1995; Lyutikov 2003) as well as FRBs (Lyutikov 2021).

Rotation-powered radio pulsars (RPPs) with high magnetic field strengths ($B \gtrsim 4.41 \times 10^{13} \text{ G}^9$) have long been anticipated to be closely related to magnetars (Ng & Kaspi 2011). Detection of magnetar-like short bursts from two of such systems; PSR J1846.4–0258 (Gavriil et al. 2008) and PSR J1119 –6127 (Gogus et al. 2016) strengthened the association of RPPs with magnetars. On the other hand, only six out of nearly 30 known magnetars have been observed to occasionally emit pulsed radio signals (Olausen & Kaspi 2014). Despite the small fraction, this also means that at least some magnetars could host an appropriate mechanism for particle acceleration

This is the magnetic field whose cyclotron energy corresponds to the rest mass energy of an electron.

http://www.physics.mcgill.ca/~pulsar/magnetar/main.html

to RPP-like radio beams. An important question that still remains is whether magnetar-like bursts in RPP-like radio beams share common characteristics with bursts from magnetars. For this purpose, we investigated spectral properties of hard X-ray bursts from two radio-loud high-B-field pulsars recently observed with Fermi-GBM.

One of the two sources, Swift J1818.0-1607, was discovered on 2020 March 12 by its emission of magnetar-like burst detected with the Burst Alert Telescope (BAT) aboard the Neil Gehrels Swift Observatory (Evans et al. 2020a). The spectrum of this burst is best described with a blackbody function at a temperature of 8.4 keV (Hu et al. 2020). Subsequent observations with NICER revealed this newly discovered magnetar candidate to have a very short spin period of 1.36 s, and an average spin-down rate of 2.5×10^{-11} s s⁻¹, implying a magnetar-level surface magnetic field strength of 2.5×10^{14} G at the equator (Hu et al. 2020). Multiwavelength radio monitoring observations also revealed pulsations from Swift J1818.0–1607 at the same spin period, making it a radioloud magnetar (Champion et al. 2020; Esposito et al. 2020). The characteristic age of ~ 300 yr implies that Swift J1818.0 -1607 is likely one of the youngest magnetars (Esposito et al. 2020). However, a recent estimate of its age using long-term monitoring observations yields that the source is slightly older: 860 yr (Rajwade et al. 2022). The distance to this source is estimated to be between 4.8 and \sim 8 kpc (Karuppusamy et al. 2020; Lower et al. 2020).

The other source of interest here is PSR J1846.4–0258, in the supernova remnant Kesteven 75. The pulsar has a spin period of 0.327 s. It is another very young system with a characteristic age of slightly over 700 yr (Gotthelf et al. 2000), powering a surrounding wind nebula (Gotthelf et al. 2021). After about 14 yr of quiescence (Blumer et al. 2021), PSR J1846.4–0258 became active again on 2022 August 1 when a short burst was detected with Swift-BAT (Krimm et al. 2020). Chandra observations following this activity revealed an emerging thermal component in the X-ray spectrum of the pulsar's persistent emission, while the emission properties of its wind nebula remained unchanged (Blumer et al. 2021). The distance to PSR J1846.4–0258 is estimated to be between 5.1 and 7.5 kpc (Leahy & Tian 2008).

Here, we present our comprehensive study of hard X-ray bursts from Swift J1818.0–1607 and PSR J1846.4–0258 detected with Fermi-GBM during their burst-active episodes in 2020–21. We searched the GBM data for untriggered bursts from these two sources using three techniques, and analyzed all identified bursts. In Section 2 below, we introduce our search and identification methodology for bursts from both sources in the continuous data. In Section 3, we present the resulting burst samples and the outcomes of time-integrated spectral investigations of these bursts. Finally, we discuss the implications of our results in Section 4.

2. Fermi-GBM Observations and Untriggered Event Identification

Fermi-GBM consists of 14 scintillator detectors: 12 sodium iodide (Na I) detectors and two bismuth germanate (BGO) detectors (Meegan et al. 2009). The Na I detectors are sensitive to photons in the energy range of ${\sim}8~\text{keV-1}$ MeV, distributed around the spacecraft in clusters, continuously monitoring the entire sky unocculted by Earth. The BGO detectors are sensitive to higher energy photons (${\sim}200~\text{keV-30}$ MeV), located on

two sides of the spacecraft. In this study, we only use the data of 12 Na I detectors since the spectral range of the magnetar (or Soft-Gamma Repeater; SGR) bursts reported in this study lies below the effective energy range of the BGO detectors.

There are three types of continuously accumulated Fermi-GBM data: CTIME data having 0.256 s time resolution in eight energy channels, CSPEC data having 8.192 s time resolution in 128 energy channels, and continuous time-tagged event (CTTE) data having $2 \mu s$ time resolution and 128 energy channels. Of those, the CTTE data type provides the finest temporal and spectral resolutions. Therefore, we used the CTTE data in our search of short, untriggered events from both magnetars. Throughout 2020–21, two other nearby sources were also active: SGR J1935+2154 in 2020 April-May and 2021 January, and SGR J1830-0605 between September 2020 and the end of 2021 January (see Figure 1). Also, one single burst from SGR 1806-20, was detected on 2020 April 30. We chose the search periods so as to minimize the overlapping time intervals with these active nearby SGRs. This is due to the fact that Fermi-GBM is not a pointing instrument and cannot provide accurate source location information. Error circles in location estimates using GBM data could include multiple SGRs (see Section 2.1 for more details on location estimation). We present in Figure 1 the burst timelines of Swift J1818.0 -1607 and PSR J1846.4-0258 along with two other nearby SGRs that were burst active in 2020. Swift trigger information is included here since Swift has an arcmin localization accuracy that enables unambiguous source identification. Additionally, we optimized our search periods for bursts from both sources by considering their activity as follows.

Swift J1818.0–1607: Fermi-GBM triggered on short bursts originating from the direction of Swift J1818.0–1607 on three days: 2020 December 13, 2021 January 6, and 2021 January 24. However, the source was found to be "burst active" by Swift much earlier in 2020 March (Evans 2020b). Therefore, the Fermi-GBM data could contain subthreshold, untriggered bursts from this source between 2020 February and 2021 January (see Figure 1).

PSR J1846.4–0258: Only one burst from the direction of PSR J1846.4–0258 triggered Fermi-GBM on 2020 August 1 at 20:11:47 UTC, which was simultaneously detected by Swift-BAT (Krimm et al. 2020). Swift-BAT detected another burst from the source on 2020 August 31, which did not trigger Fermi-GBM although the source was visible to Fermi at the time of the BAT trigger (the burst is seen in the lightcurve of only one of the 12 GBM detectors); therefore, it is possible that we find untriggered bursts within the GBM data around the month of August.

Therefore, we performed extensive blind searches for short bursts among the data of 2020 February through 2021 January in order to uncover additional bursts from these two sources that did not trigger GBM (Figure 1). We employed three different techniques to search for bursts, with an energy range and a time resolution specifically aimed at finding SGR bursts. The search results were then subjected to an identification algorithm, which estimates the probability for a certain event type and a possible source location for each event. The burst search method and event-classification process are described in detail in the Appendix. Below, we describe our event localization methodologies in detail.

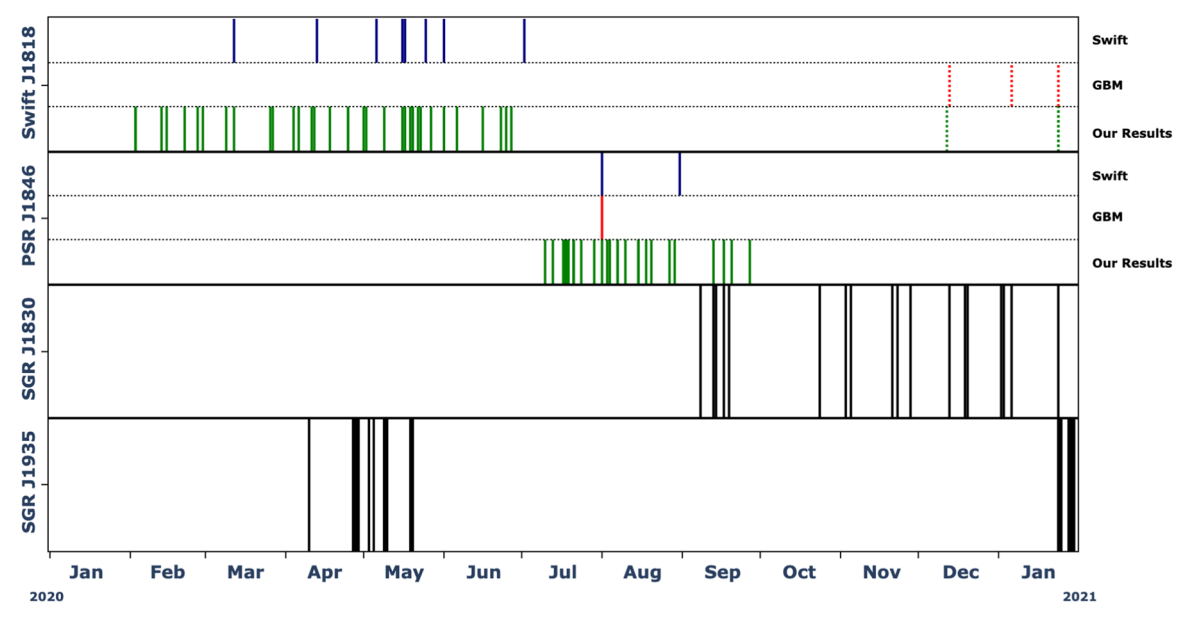


Figure 1. Burst timeline of Swift J1818.0–1607 and PSR J1846.4–0258 along with two nearby SGR sources that were active in 2020 and January 2021, showing the days on which bursts were detected from each source. Green lines represent untriggered events identified in this work. The bursts from SGRs J1935+2154 (Lin et al. 2020a) and J1830–0605 (L. Lin et al. 2022, in preparation, O. J. Roberts et al. 2022, in preparation) are shown in black lines. Events detected with Swift-BAT and Fermi-GBM are indicated with blue and red colors, respectively. Dotted lines in 2020 December to January represent bursts from either Swift J1818.0–1607 or SGR J1830–0605 (the exact origin cannot be identified). We also note that a single burst from another nearby source, SGR 1806–20, was detected on 2020 April 30 by both Swift-BAT and Fermi-GBM (Ambrosi et al. 2020; Malacaria & Fermi GBM Team 2020). (References: Barthelmy et al. 2020; Bernardini et al. 2020; Evans 2020b; Gronwall et al. 2020)

2.1. Candidate Event Localization

In order to identify an event as a short burst originating from one of the two sources under investigation here, one needs to determine both the location and the type of the event. How we determined the types of the candidate events found in the search are described in the Appendix. Here, we describe our approaches for localizing the candidate events that resulted in high probability of being SGR bursts. GBM is an all-sky monitor and does not have a precise localization capability. However, a rough estimate of the event location could be inferred from the correlations between the peak count rates and detector-to-source angles (θ) of all 12 detectors at the time of the event. Therefore, we looked for a positive correlation between the cosines of θ and the corresponding peak count rates (in log scale), assuming the source location at the positions of Swift J1818.0-1607 and PSR J1846.4-0258. The correlation was determined with linear fits, using all detectors with $\theta \le 60^{\circ}$. We note that we took into account possible blockage of detector's field of view by other parts of the spacecraft, 11 and used only unblocked detectors for this analysis. As an added measure, all the events that resulted in a well-constrained positive trend were subjected to a more detailed localization algorithm developed by the GBM team (Kocevski et al. 2018; Goldstein et al. 2019), using several spectral templates, which include a blackbody spectral template with a fixed temperature (kT = 10 keV). This "targeted search" (Kocevski et al. 2018; Goldstein et al. 2019) is a subthreshold algorithm initially developed to identify and recover weak short gamma-ray bursts (GRBs) below the on-board trigger

threshold, possibly associated with gravitational wave events. The algorithm is currently being adapted to search for other transients such as SGR bursts, for which the blackbody spectral template has recently been added. The search uses a set of discrete timescales for a duration over which the log-likelihood ratio of a subthreshold event is maximized, calculated by comparing the presence of a signal to the null hypothesis of pure background. The spectral templates are folded through the GBM detector responses to provide an estimated count spectrum of the transient at a certain location. The event localization is done by calculating and combining the estimated expected count rate with each spectral template, comparing them to the observed counts for each grid-point on the sky. The localization errors vary depending on the significance of the event, but generally cover several tens to hundreds of square degrees on the sky. For our candidate events, we used the targeted search algorithm for localization purpose only, for the specific time of each candidate event. The duration of each event was taken as the default timescale for this process.

In Figure 2, we present the localization results of our candidate events for both Swift J1818.0–1607 and PSR J1846.4 -0258, along with the locations of nearby SGRs. While it is not currently optimized to localize much-softer and dimmer SGR bursts, the targeted search results for most of the events in our sample (with the $\cos \theta$ -peak counts positive trends) were within the expected error region around the location of Swift J1818.0–1607 and PSR J1846.4–0258. There were some weak events (\sim 6% of our sample) for which the targeted search was not able to localize within the expected error region of either source, as can be seen in Figure 2. These events were not excluded from our list, however, since no definitive association to any source could be obtained solely with the localization algorithm due to the limitations of GBMs design as a monitoring detector. Among our candidates, all GBM-triggered events classified by the GBM team as SGR were identified to

¹¹ Some GBM detectors' views can be partially blocked by a part of the spacecraft for a particular source direction, depending on the orientation of the spacecraft at the time of the observation. Therefore, we checked whether any detectors were partially or fully blocked by the LAT detector at the trigger time using the GBMBLOCK software provided by the GBM team.

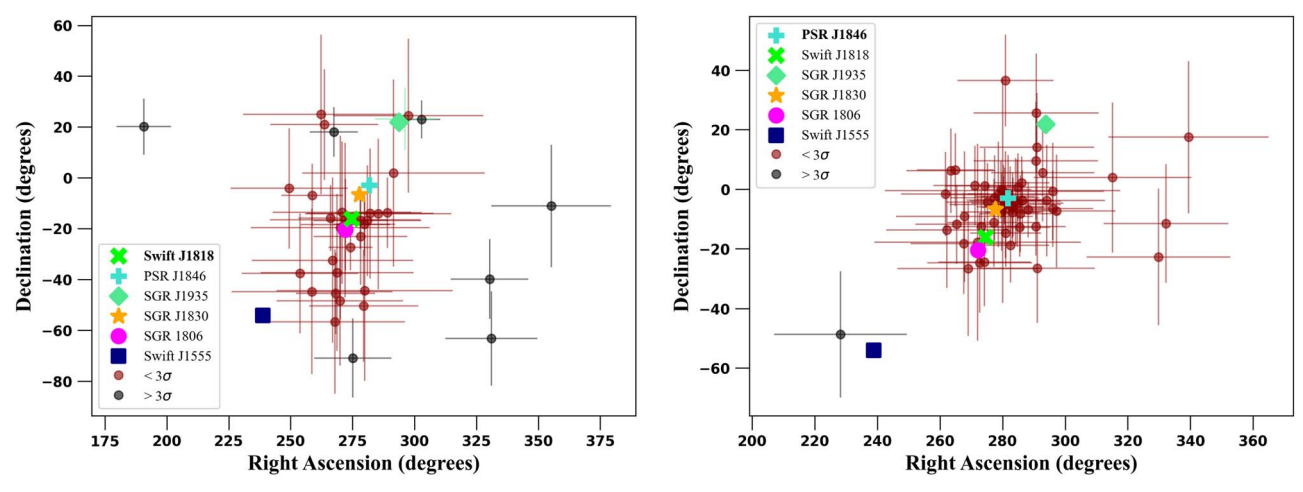


Figure 2. Localization results of the candidate events for Swift J1818.0–1607 (left) and PSR J1846.4–0258 (right) along with the locations of nearby SGR sources. The 1σ uncertainties are shown. The events localized within 3σ the corresponding source position are shown in dark red while those localized more than 3σ away are shown in gray.

have originated from the direction of either Swift J1818.0 -1607 or PSR J1846.4-0258 based on our localization estimates described above.

3. Burst Search Results and Spectral Analysis

Through our search, we identified a total of 37 and 58 SGR bursts likely originating from Swift J1818.0-1607 and PSR J1846.4–0258, respectively. We list in Tables 1 (for Swift J1818.0-1607) and 2 (for PSR J1846.4-0258), the times of the identified events, along with the detectors that they have been detected with, event duration, as well as search methods that they have been identified with. Also in Tables 1 and 2, S/ N of all the bursts are listed; note that many of the untriggered events are naturally dim, indicated by the S/N. In these tables, we also indicate the poorly localized events (see Section 2.1). As mentioned earlier, our searches identified all the triggered bursts that were localized to the directions of Swift J1818.0 -1607 or PSR J1846.4-0258 during the search periods (see Figure 1). In particular, our results indicated that burst activity of Swift J1818.0-1607 ceased near the end of 2020 June and the active episode of PSR J1846.4-0258 starts around the middle of 2020 July. As an independent diagnostic, we investigated all pointed NICER observations of Swift J1818.0 -1607 from 2020 June 1 through 2020 July 26. 12 We generated their light curves in the 1-10 keV band with a time resolution of 0.01 s and inspected them for burst events. We find that Swift J1818.0-1607 was burst silent in most of these pointed observations. The only burst from this source seen with NICER in this time interval was on 2020 June 14 at 03:57:26.7 UTC. Another important fact is that the persistent X-ray emission of PSR J1846.4-0258 was already higher than its long-term quiescent level by a factor of four after 2020 June 26 and by a factor of ten after July 25 (Kuiper et al. 2020). Based on these facts, we attribute the events that we found in 2020 July to PSR J1846.4-0258. In Figure 3, we present the GBM lightcurve of a 1600 s long segment during which 17 bursts

were identified from PSR J1846.4–0258, which is the most burst-dense time period for PSR J1846.4–0258 in 2020.

We add a caveat here that due to the spatial proximity and the closeness of their active periods, some of the identified events in early 2020 July could still be originating from Swift J1818.0–1607. Similarly, the time of three bursts seen in 2020 December/2021 January coincide with the active period of another nearby source, SGR J1830–0605. Therefore, we cannot unambiguously associate these events (S35–S37) with Swift J1818.0–1607. We did investigate these three events but we do not include their properties in determining collective or average characteristics of Swift J1818.0–1607 bursts. Moreover, we note that the exclusion of the poorly localized events in our sample (indicated in the tables) did not alter our analysis results for the collective properties of the two sources.

3.1. Burst Duration

Event-duration calculations were done as a part of the eventclassification process, as described in the Appendix. To recap the duration-calculation method, the light curves of the two brightest detectors without any spacecraft blockage were combined for each event and the duration was determined by generating Bayesian block representations of the lightcurve with 1 ms time resolution in the energy range of 10-100 keV. We find that duration of Swift J1818.0-1607 events range from 5 to 449 ms with an average duration of 49.4 ms. For PSR J1846.4-0258, burst duration range from 3 to 183 ms with an average of 26.3 ms (see Tables 1 and 2). We note that many of the shortest events (\sim 8 ms) are the ones identified only by S/N and/or Poisson statistics search methods, which use the data with fixed time steps of 8 ms. Additionally, some of those short events are weak and the duration could not be determined with the 1 ms combined lightcurve. In such cases, we used the search time resolution of 8 ms as the duration upper limit for those bursts.

3.2. Spectral Analysis

We performed time-integrated spectral analysis of each of these bursts with RMFIT (version 4.3.2)¹³ using Castor statistics (C-stat). For the analysis, we used the CTTE data binned to

¹² There are 23 observations with observation IDs: 3556013301, 3556013302, 3556013401, 3556013501, 3556013502, 3556013601, 3556013701, 3556013801, 3556013901, 3556014001, 3556014101, 3556014102, 3556014201, 3556014301, 3556014302, 3556014401, 3556014501, 3556014701, 3556014802, 3556014901, 3598010801, 3598010802.

¹³ Astrophysics Source Code Library, record ascl:1409.011, Gamma-ray astronomy Group, University of Alabama in Huntsville.

Table 1Swift J1818.0–1607 Events Identified in Our Search

ID	Event Time (UTC)	Time (Fermi MET)	Detectors ^a	Duration	Search Method ^b	S/N ^c
	(YYMMDD hh:mm:ss)	(s)		(ms)		,
S1 T _F	200203 03:17:11.908	602392636.908	0,1,2,3,5	66	1	15.8
S2	200203 17:52:15.575	602445140.576	0,1,2,5	8	1,2,3	12.2
S3	200213 02:56:04.468	603255369.469	0,1,3,5	8	1	9.7
S4	200215 10:10:59.453	603454264.454	0,1,2,5	8	2	6.1
S5	200222 15:26:29.970	604077994.970	0,1,3	9	2	4.7
S6 ^e	200227 09:59:12.821	604490357.821	3, 4	8 ^d	2	5.4
S7	200229 18:56:16.643	604695381.644	3,4	14	1,2,3	13.4
S8	200309 13:59:01.521	605455146.521	0,1,2,9	17	3	8.3
S9 T_S	200312 21:16:47.328	605740612.329	0,1,3,6,9	17	1,2,3	10.8
S10	200326 16:26:12.425	606932777.426	2,10	8 ^d	3	5.4
S11	200327 13:21:42.573	607008107.574	3,4	449	1	8.2
S12 ^e	200404 21:19:24.252	607727969.252	4,7,8	6	3	5.5
S13 ^e	200406 12:37:49.372	607869474.372	2,10	3	3	5.8
S14	200411 20:15:40.989	608328945.989	8	5	2,3	6.3
S15	200412 04:06:10.872	608357175.872	6,7	8 ^d	3	4.6
S16	200418 00:09:24.886	608861369.886	9 ,10	9	1	8.9
S17	200425 06:34:44.643	609489289.643	9,10	5	2,3	10.9
S18 ^e	200425 20:20:59.720	609538864.720	7 ,8	8 ^d	2	5.7
S19	200501 15:35:28.235	610040133.236	9, 10 ,11	440	1,3	8.9
S20	200502 09:22:51.711	610104176.712	7,8	8 ^d	2	5.9
S21 ^f	200509 12:57:57.391	610721882.391	6,7, 11	8 ^d	2	5.2
S22	200516 15:49:32.484	611336977.485	8,11	8 ^d	2	5.9
S23	200517 14:29:54.281	611418599.281	6,7,8	8	2	6.4
S24	200519 07:15:32.836	611565337.837	8,11	8	2	6.5
S25	200520 10:23:51.123	611663036.124	9 ,10,11	7	3	6.1
S26	200522 19:58:13.477	611870298.478	6,7, 9	5	2	6.0
S27	200523 08:32:33.465	611915558.465	6,7, 9 ,10,11	5	1	4.6
S28	200527 11:59:42.267	612273587.267	9,10, 11	9	2,3	10.1
S29 ^e	200601 03:32:30.056	612675155.056	8,11	8	3	6.4
S30	200606 13:35:26.048	613143331.048	8,11	9	3	6.1
S31	200616 19:08:30.751	614027315.752	7,8,11	8	3	5.9
S32	200623 10:00:45.970	614599250.971	7,11	6	2,3	6.4
S33	200625 16:01:32.086	614793697.086	7, 9 ,11	9	2	6.8
S34	200627 23:51:48.891	614994713.892	6,7,8,9,10, 11	221	1,3	10.1
S35 ^e , ^g	201212 02:33:34.061	629433219.062	1 ,3 ,5	10	2	6.0
S36 ^g	210124 19:13:48.229	633208433.230	0,1,5	10	3	5.9
S37 ^e , ^g	210124 20:48:23.943	633214108.943	0,1,3,4	40	1,2,3	22.2

Notes.

8 ms resolution. All unblocked detectors with θ < 60° between the detectors' zenith to sources at the time of the event were included in the analysis. The background count rates were modeled with a linear function for each detector based on the \sim 50 s data segments before and after the burst. We then generated detector response matrices (DRMs) with GBM Response Generator provided by the Fermi-GBM team, for corresponding source locations. The time interval used in the analysis covers the entire duration of the event, and the energy range of $8-200 \ \text{keV}$ was used for all events.

As described earlier, the GBM data do not allow for localization beyond an accuracy of a few degrees, and resolving the

nearby sources becomes a challenge when multiple nearby SGRs are simultaneously burst active. For some of the events listed in Table 1, we could not definitively identify the source, which was stated as a caveat at the beginning of this section. To assess how the uncertainties in the event localization may affect our analysis results, we first selected a random subset of the events and generated DRMs with two source locations for each event time: one with Swift J1818.0–1607 and the other with PSR J1846.4–0258. We then fitted their spectra with a set of photon models (described below) using both DRMs and compared the spectral parameters. We found that, for all of the subset events, the spectral parameters were consistent within 1σ

 T_F Fermi/GBM-triggered bursts.

TS Swift/BAT triggered bursts.

^a Unblocked detectors with <60° detector zenith-to-source angle used in spectral analysis. The brightest detectors are shown in bold.

^b Methods by which the events were found. 1, Bayesian: 2, Poisson; 3, S/N.

 $^{^{\}rm c}$ Signal-to-noise ratio of bursts calculated for whole duration in the energy range of 10–100 keV with two brightest detectors.

^d Duration cannot be determined by Bayesian method with combined lightcurve. Search time resolution (8 ms) multiplied by the number of burst time bins identified in our search were used as duration.

^e Our best localization is more than 3σ away from Swift J1818.0–1607.

f Could be originating from either Swift J1818.0-1607 or SGR J1935-2154.

g Could be originating from either Swift J1818.0–1607 or SGR J1830–0605.

Table 2PSR J1846.4-0258 Events Identified in Our Search

ID	Event Time (UTC) (YYMMDD hh:mm:ss)	Time (Fermi MET) (s)	Detectors ^a	Duration (ms)	Search Method ^b	S/N ^c
P1	200710 04:59:48.361	616049993.361	7,11	10	2	5.9
P2	200713 05:43:39.507	616311824.507	7,8,11	12	2,3	10.4
P3	200717 17:53:31.999	616701216.999	7,8,11	10	2	6.5
P4 ^T F	200718 08:24:38.725	616753483.725	6,7, 9 ,10,11	183	1,3	12.0
P5	200718 08:25:05.958	616753510.958	6,7,9,10, 11	74	1,2,3	15.3
P6	200718 08:26:11.287	616753576.287	7,9,10, 11	30	1,2,3	18.7
P7	200718 08:26:40.698	616753605.698	7,9, 10 ,11	44	1,2,3	22.1
P8	200718 08:26:50.509	616753615.509	7,9,10, 11	7	12	8.0
P9	200718 08:31:11.524	616753876.524	9,10, 11	44	1,2,3	17.4
P10	200718 08:39:56.890	616754401.890	9,10, 11	11	1,2,3	16.5
P11	200718 08:40:34.580	616754439.580	9,10,11	78	1	8.6
P12	200718 08:40:50.348	616754455.348	9,10, 11	27	1,2,3	10.4
P13	200718 08:41:02.806	616754467.806	9, 10 ,11	9	2,3	8.4
P14	200718 08:41:04.962	616754469.962	9, 10 ,11	16	1,2,3	18.6
P15	200718 08:41:51.706	616754516.706	9,10, 11	22	1,2,3	27.2
P16	200718 08:43:04.386	616754589.386	9,10, 11	31	1,2,3	13.4
P17 T_F	200718 08:43:47.599	616754632.599	10 ,11	133	1,2,3	52.5
P18	200718 08:44:04.331	616754649.331	10 ,11	6	1,2,3	10.9
P19	200718 08:47:54.141	616754879.141	10 ,11	16	1,2,3	22.6
P20	200718 08:48:51.071	616754936.071	10 ,11	122	1,2,3	27.1
P21	200718 09:53:58.478	616758843.478	6,7, 9 ,10,11	14	1,2,3	9.9
P22	200718 09:56:03.452	616758968.452	6,7,9,10, 11	14	1,2,3	12.7
P23	200718 10:06:41.223	616759606.223	9, 10 ,11	25	1,2,3	13.5
P24	200718 10:07:53.283	616759678.283	9,10,11	20	2,3	9.7
P25	200718 10:11:04.196	616759869.196	9,10,11	7	1,2,3	6.9
P26	200718 11:12:11.076	616763536.076	6,7,8,9,11	5	3	11.4
P27	200718 11:39:57.349	616765202.349	9,10,11	30	1,3	9.4
P28	200718 14:35:42.363	616775747.363	6,7,9,10, 11	11	1	11.6
P29 T _F	200718 14:50:52.381	616776657.381	7, 9 ,10,11	53	1,2,3	43.7
P30	200718 14:50:54.393	616776659.393	7,9,10, 11	30	1,2,3	13.4
P31	200718 14:51:10.244	616776675.244	7,9,10, 11	46	1,2,3	16.7
P32	200718 14:57:18.377	616777043.377	9, 10 ,11	18	1,2,3	15.3
P33	200718 15:01:09.771	616777274.771	9,10, 11	68	1,2,3	13.5
P34	200718 15:59:04.615	616780749.615	7,8, 9 ,11	8	2,3	10.6
P35	200718 17:41:10.233	616786875.233	7,8,9,10, 11	30	1	10.1
P36	200718 22:32:03.837	616804328.837	6,7,9, 10 ,11	18	1,2,3	7.6
P37	200719 02:11:01.208	616817466.209	10 ,11	19	1,2,3	15.5
P38	200721 07:39:07.355	617009952.355	7,9,10, 11	10	1,2,3	12.4
P39	200721 08:07:14.751	617011639.751	10 ,11	4	2	6.1
P40	200724 03:30:49.443	617254254.443	7 ,8 ,11	12	1,2,3	24.3
P41	200729 16:57:18.588	617734643.588	7 ,11	8	2	6.9
P42 TF	200801 20:11:47.639	618005512.639	9, 10 ,11	20	1,2,3	15.8
P43	200803 16:44:44.978	618165889.978	8,11	8 ^d	2,3	6.0
P44	200804 16:24:05.600	618251050.600	9, 10 ,11	10	3	6.5
P45	200807 05:53:41.102	618472426.102	6,7	8 ^d	2	5.5
P46 ^t	200807 22:14:11.289	618531256.289	8,11	8 ^d	3	5.9
P47	200810 16:50:33.485	618771038.485	8 ,11	7	2	6.8
P48	200815 15:29:09.869	619198154.869	0,9	17	2	8.0
P49	200815 16:37:19.845	619202244.845	7 ,8 ,11	6	2	7.6
P50	200818 17:58:41.728	619466326.728	7, 8 ,11	8	2	6.1
P51	200820 17:27:43.283	619637268.283	6,7,8,11	8	2	6.6
P52	200827 04:59:46.160	620197191.160	7,8	7	3	5.7
P53	200829 04:42:23.203	620368948.203	6,7 ,8	8 ^d	2	5.3
P54 ^e , ^g	200913 10:53:12.824	621687197.824	6,7	8 ^d	3	5.5
P55	200917 04:06:56.137	622008421.138	3,6	10	2	7.0
P56	200917 04:08:31.609	622008516.609	0,3,6	10	3	5.3
P57	200920 02:01:12.821	622260077.821	0,3,6	3	3	5.5
P58	200927 19:48:44.762	622928929.762	3,4,7, 8	8	2,3	8.0

Notes.

 T_F Fermi/GBM-triggered bursts.

T_S Swift/BAT triggered bursts.

 $^{^{}a}$ Unblocked detectors with $<60^{\circ}$ detector zenith-to-source angle used in spectral analysis. The brightest detectors are shown in bold.

b Methods by which the events were found. 1, Bayesian; 2, Poisson; 3, S/N.

c Signal-to-noise ratio of bursts calculated for whole duration in the energy range of 10–100 keV with two brightest detectors.

d Duration cannot be determined by Bayesian method with combined lightcurve. Search time resolution (8 ms) multiplied by the number of burst time bins identified in our search were used as duration.

 $^{^{\}rm e}$ Our best localization is more than 3σ away from PSR J1846.4–0258.

 $^{^{\}rm f}$ Could be originating from either PSR J1846.4–0258 or SGR J1935–2154.

^g Could be originating from either PSR J1846.4-0258 or SGR J1555-5402.

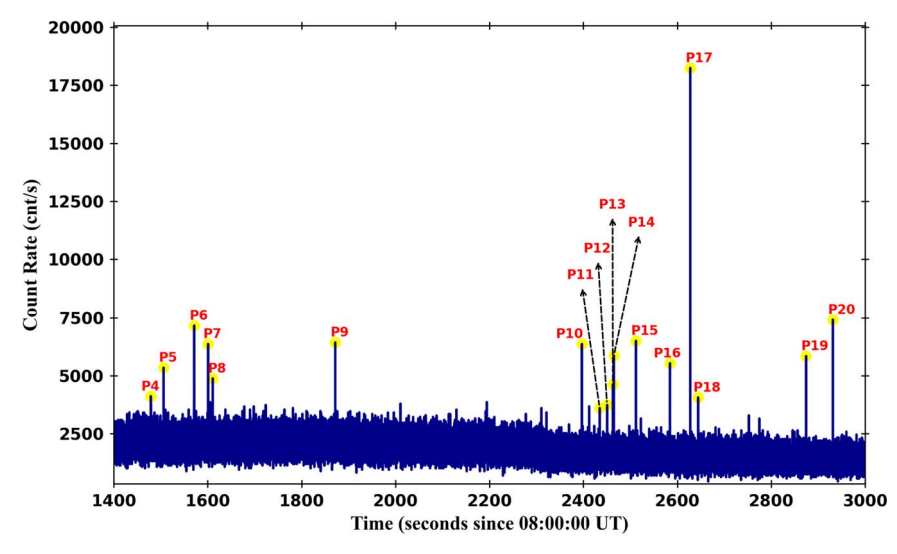


Figure 3. GBM lightcurve (10–100 keV) for the eighth hour of 2020 July 18, on which multiple bursts are observed, likely coming from PSR J1846.4–0258. It is produced using the events from the two brightest detectors (Na I 10 and 11) binned with 16 ms resolution. The event designations in Table 2 are labeled.

uncertainties; thus, we conclude that the localization uncertainties do not play a crucial role in our analysis in terms of individual spectral parameters obtained. We note, however, that when the DRMs were generated with a location of another SGR that is sufficiently far (such as SGR 1935+2154), the spectral parameters become inconsistent.

We fit each burst spectrum with three photon models that are known to best describe magnetar bursts: Comptonized model (COMPT; $f(E) = A \exp[-E(2 + \alpha)/E_{\text{peak}}](E/50 \text{ keV})^{\alpha}$, where E_{peak} is the energy at which νF_{ν} spectrum peaks), single blackbody function (BB), and the sum of two blackbody functions (BB+BB). The spectral parameters were obtained by minimizing C-stat (i.e., maximizing the likelihood), and we considered that the fitted model describes the spectra sufficiently well if all parameters are constrained to <30% of the parameter value by the upper 1σ uncertainties. In case of the photon index parameter (α) of the COMPT model, we used the constraint criteria of e-folding energy, $E_0 = E_{\text{peak}}/$ $(2 + \alpha) \gtrsim 20$ keV, which is well above the lower-energy bound of our data, ensuring that sufficient amount of data exist to determine α . We then calculated photon flux and energy flux of each burst in 8-200 keV energy range based on the well-constrained fits.

We find the spectra of all bursts from Swift J1818.0 -1607 are adequately modeled with a single BB function. The resulting weighted average of blackbody temperature of these bursts is 7.83 ± 0.25 keV. Note that spectra of five (14%) Swift J1818.0–1607 bursts can also be modeled well with COMPT, yielding weighted average values for the power-law index α of -0.51 ± 0.54 and $E_{\rm peak}$ of 37.96 ± 4.54 keV. Similarly for PSR J1846.4-0258, all 58 spectra can also be described with a single BB with a weighted mean kT of 11.14 ± 0.15 keV. Moreover, the COMPT model fits the spectra of 20 (34%) of PSR J1846.4–0258 bursts equally well. The weighted averages of the COMPT parameters for this subset of events are $\alpha = -0.16 \pm 0.13$ and $E_{\rm peak} = 45.91 \, \pm \, 1.11$ keV. In Tables 3 and 4, we present the fit results as well as bursts fluences for all events we identified. The fit statistic used here, C-stat, is a maximum likelihood statistic and does not determine the goodness of fit. Therefore, to determine the statistically preferred model among the two, we calculated the Bayesian Information Criterion (BIC) (Liddle 2007), which is a function of the C-stat value and the degrees of freedom, for each fit. The COMPT was considered the preferred model when ${\rm BIC_{BB}} - {\rm BIC_{COMPT}} > 10$. The preferred models are also indicated in the Tables 3 and 4 where applicable. In many cases, the differences in BIC were small, meaning that the both models describe the spectra equally well. While calculating fluences of these events, we used energy flux values of the preferred model.

4. Discussion

A radio-loud magnetar Swift J1818.0–1607 was discovered in early 2020 with magnetar-like bursts detected with Swift. The other source of our interest, PSR J1846.4-0258, emitted several magnetar-like bursts in 2006 while exhibiting characteristic behavior of a rotation-powered pulsar with high magnetic field (Gavriil et al. 2008). After 14 yr of burst quiescence (Blumer et al. 2021), the source broke its silence and became burst active again also in 2020. Our deep search in the Fermi-GBM database for weaker bursts from these two sources resulted in identifying 95 events including the triggered ones coming from Swift J1818.0-1607 and PSR J1846.4 -0258. Here, we compare the results of our temporal and spectral investigations of bursts with one another, as well as burst characteristics of other magnetars, in particular, SGR J1550-5418 and SGR J1935+2154, which are among the pulsed radio-emitting systems.

We first present burst duration and flux information for both sources in Figure 4. We find that the burst fluxes from both sources span nearly the same range; from 10^{-7} to 2×10^{-6} erg cm⁻² s⁻¹, while the average flux of PSR J1846.4–0258 bursts are slightly higher than that of Swift J1818.0–1607 bursts $(5.1\times10^{-7}~{\rm erg}~{\rm cm}^{-2}~{\rm s}^{-1}~{\rm for}~{\rm Swift}~{\rm J1818.0}-1607~{\rm and}~7.5\times10^{-7}~{\rm erg}~{\rm cm}^{-2}~{\rm s}^{-1}~{\rm for}~{\rm PSR}~{\rm J1846.4}-0258~{\rm bursts}).$

We also find that the burst duration spans a similar range for both of the sources, and Swift J1818.0–1607 events with mean duration of 49.4 ms are comparable to the PSR J1846.4 -0258 events with mean duration of 26.3 ms. However, the duration of these bursts in our sample are noticeably shorter for both Swift J1818.0–1607 and PSR J1846.4–0258 in comparison to the duration of the bursts from other magnetars:

Table 3Spectral Fit Results of Swift J1818.0–1607 Bursts

	BB			COMPT		
ID	kT (keV)	C-Stat/DoF	$E_{ m peak} \ m (keV)$	Index	C-Stat/DoF	Fluence ^a , ^b (10 ⁻⁸ erg cm ⁻²)
S1 T _F	$11.2^{+0.6}_{-0.6}$	375.0/338				5.62 ± 0.40
S2	$7.8^{+1.2}_{-1.1}$	178.7/270	30.2 ± 6.9	-0.6 ± 1.0	175.4/269	1.00 ± 0.15
S3	$5.8^{+0.8}_{-0.7}$	238.8/269				0.62 ± 0.08
S4	$10.0_b^{+4.1}$	194.4/269				0.16 ± 0.06
S5	$18.0_b^{+6.8}$	196.0/201				0.25 ± 0.09
S6	$6.7_b^{+8.7}$	97.7/135				0.42 ± 0.14
S7	$7.7^{+0.9}_{-0.8}$	112.6/135				1.64 ± 0.24
S8	$17.6^{+4.1}_{-3.1}$	300.3/269	72.2 ± 17.8	0.7 ± 1.6	300.2/268	0.74 ± 0.19
S9 T_S	$6.3^{+1.0}_{-0.8}$	285.5/338				0.99 ± 0.14
S10	$3.7_{h}^{+1.5}$	109.4/133				0.15 ± 0.05
S11	$3.9^{+0.6}_{-0.5}$	130.4/135				4.63 ± 0.67
S12	$13.3^{+3.1}_{-2.7}$	164.4/204	52.8 ± 12.6	0.6 ± 1.8	164.1/203	0.33 ± 0.08
S13	$15.6_b^{+4.2}$	128.4/133				0.13 ± 0.04
S14	$19.1_b^{+8.3}$	45.1/66				0.19 ± 0.09
S15	$12.3_b^{+5.0}$	130.2/136				0.22 ± 0.08
S16	$8.9^{+2.1}_{-2.0}$	132.8/133				0.61 ± 0.13
S17	$9.4^{+1.9}_{-1.6}$	124.5/133				0.23 ± 0.06
S18	$6.7^{+2.2}_{-2.2}$	89.9/135				0.51 ± 0.14
S19	$10.3^{+0.9}_{-0.8}$	237.9/202				7.33 ± 0.88
S20	$6.5^{+2.5}_{-1.6}$	82.3/135				0.45 ± 0.14
S21	$8.9^{+3.1}_{-2.6}$	143.0/205				0.47 ± 0.14
S22	$11.9_b^{+4.4}$	116.8/135				0.24 ± 0.10
S23	$13.5^{+3.8}_{-2.8}$	169.2/204				0.63 ± 0.17
S24	$18.5^{+3.8}_{-3.0}$	89.3/135				0.92 ± 0.26
S25	$7.8_b^{+3.8}$	171.9/202				0.13 ± 0.05
S26	$7.3_{-1.4}^{+1.7}$	139.1/204				0.33 ± 0.08
S27	$10.1^{+1.8}_{-1.5}$	307.2/340				0.17 ± 0.04
S28	$11.4_b^{+4.3}$	170.4/202				0.35 ± 0.14
S29	$17.9^{+3.5}_{-2.8}$	110.0/135				0.98 ± 0.26
S30	$7.3_b^{+2.1}$	104.4/135				0.30 ± 0.10
S31	$12.1_b^{+4.7}$	175.4/204				0.20 ± 0.08
S32	$11.7^{+2.3}_{-1.8}$	108.4/136				0.55 ± 0.15
S33	$14.4^{+4.5}_{-3.7}$	190.8/204				0.41 ± 0.13
S34	$10.3^{+1.1}_{-1.1}$	479.0/408	40.2 ± 6.4	-0.7 ± 0.7	471.9/407	4.71 ± 0.51
S35	$6.6_b^{+5.9}$	171.2/201				0.10 ± 0.07
S36	$12.2^{+3.5}_{-2.7}$	167.2/201				0.47 ± 0.13
S37	$9.5^{+0.8}_{-0.7}$	370.9/270	36.3 ± 5.8	-1.0 ± 0.5	360.3/269	3.55 ± 0.32

Notes. Bold entries represent the statistically preferred model determined by ΔBIC . Uncertainties are 1σ .

For example, the mean duration SGR J1935+2154 bursts in its 2019–2020 activity episode was 169 ms (Lin et al. 2020a) and that of SGR J1550–5418 bursts in 2008–2009 was \sim 170 ms (van der Horst et al. 2012; von Kienlin et al. 2012). However, bursts from Swift J1818.0–1607 and PSR J1846.4–0258 studied here are less energetic than those of SGR J1935+2154 (Lin et al. 2020a) and SGR J1550–5418 (Lin et al. 2012). For a fair comparison, considering only the bursts from these two other magnetars in the flux interval of Swift J1818.0–1607 and PSR J1846.4–0258 events (that is, between 1×10^{-7} and 2×10^{-6} erg cm⁻² s⁻¹); we obtain a mean duration of 140 ms for SGR J1935+2154 bursts in its

2014–2016 activity (Lin et al. 2020b) and 303 ms with bursts seen in 2019–2020 (Lin et al. 2020a). The mean duration of SGR J1550–5418 bursts within the same flux range seen in the 2008–2009 active episode was 236 ms (von Kienlin et al. 2012). We conclude that the duration of Swift J1818.0 –1607 and PSR J1846.4–0258 bursts are on average shorter than those of prolific and pulsed radio-emitting magnetars. This signals a lower net energy release for these high-field sources relative to general magnetars, a property that could serve as a distinction between these two classes of neutron stars.

In addition, we constructed the time evolution of cumulative burst fluence for both sources, which we present in Figure 5.

T_F Bursts triggered Fermi/GBM.

T_S Bursts triggered Swift/BAT.

^a Calculated in 8-200 keV.

^b Negative error cannot be determined.

Table 4Spectral Fit Results of PSR J1846.4–0258 Bursts

	ВВ		COMPT			
ID	kT	C-Stat/DoF	$E_{ m peak}$ (keV)	Index	C-Stat/DoF	Fluence ^a , ^b
	(keV)		(keV)			$(10^{-8} \text{ erg cm}^{-2})$
P1	$12.7^{+3.0}_{-2.4}$	105.6/136				0.55 ± 0.16
P2	$7.1^{+0.9}_{-0.8}$	161.1/204				0.89 ± 0.12
P3	$6.1_b^{+1.7}$	170.3/204				0.23 ± 0.07
P4 T_F	$11.7^{+1.0}_{-0.9}$	428.6/340				4.87 ± 0.49
P5	$9.5^{+0.7}_{-0.6}$	317.9/340				3.36 ± 0.30
P6	$11.5^{+0.8}_{-0.8}$	290.3/272	47.3 ± 4.7	-0.4 ± 0.5	279.5/271	2.99 ± 0.25
P7	$13.5^{+0.8}_{-0.8}$	287.9/272				4.44 ± 0.33
P8	$8.1^{+1.3}_{-1.1}$	261.8/272				0.29 ± 0.05
P9	$12.3^{+1.0}_{-0.9}$	216.3/203				3.49 ± 0.35
P10	$13.4^{+1.4}_{-1.3}$	203.5/202	53.9 ± 8.5	-0.2 ± 0.8	198.8/201	1.01 ± 0.13
P11	$12.4^{+1.3}_{-1.2}$	228.0/202				3.76 ± 0.51
P12	$18.3^{+3.4}_{-3.1}$	236.2/203				1.83 ± 0.32
P13	$16.4^{+2.9}_{-2.5}$	191.2/202	67.2 ± 18.0	0.2 ± 1.2	190.3/201	0.65 ± 0.14
P14	$10.6^{+1.4}_{-1.2}$	217.1/202	55.2 ± 14.1	-1.1 ± 0.6	210.1/201	1.20 ± 0.16
P15	$11.2^{+0.9}_{-0.8}$	208.5/202	40.4 + 0.6	0.0 1.0 0	202 (/201	2.15 ± 0.22
P16	$10.2^{+1.4}_{-1.3}$	211.7/202	40.4 ± 8.6	-0.9 ± 0.8	203.6/201	1.78 ± 0.24
P17 T _F	$11.3^{+0.4}_{-0.4}$	157.6/134	$45.6^{+2.5}_{-2.2}$	$-0.01 {}^{+0.3}_{-0.3}$	138.1/133	$18.95 \pm 1.02^{\circ}$
P18	$14.2^{+2.5}_{-2.2}$	126.7/134	58.5 ± 11.1	0.4 ± 1.3	125.7/133	0.67 ± 0.14
P19	$9.0^{+1.3}_{-1.2}$	141.5/134	440 + 2.5	0.2 + 0.5	127.0 /122	1.60 ± 0.24
P20	$11.2^{+0.7}_{-0.6}$	143.7/134	44.9 ± 3.5	0.2 ± 0.5	137.9/133	9.68 ± 0.74
P21	$15.1^{+1.6}_{-1.4}$	340.7/340	59.8 ± 6.7	0.9 ± 0.9	340.1/339	0.88 ± 0.11
P22	$11.3^{+1.1}_{-1.0}$	306.9/340	45.1 5.0	02 07	100.2 /201	1.18 ± 0.14
P23 P24	$11.0^{+1.1}_{-1.0}$	203.7/202	45.1 ± 5.9	-0.3 ± 0.7	198.2/201	2.42 ± 0.28
	$12.3_{-1.5}^{+1.7} \\ 12.7_{-1.5}^{+1.7}$	197.4/202	40.0 9.7	04 12	100 1 /201	1.46 ± 0.24
P25 P26	$9.7^{+1.5}_{-1.3}$	188.7/202 291.7/341	49.9 ± 8.7	0.4 ± 1.2	188.1/201	0.74 ± 0.13 0.27 ± 0.04
P27	$12.4^{+1.3}_{-1.2}$	198.0/202				0.27 ± 0.04 1.76 ± 0.26
P28	$12.4_{-1.2}$ $14.8_{-1.5}^{+1.7}$	309.0/340	58.9 ± 9.6	0.1 ± 0.9	307.1/339	0.84 ± 0.12
$P29^{T_F}$	$10.8^{+0.4}_{-0.4}$	297.7/271	$42.5^{+2.1}_{-2.0}$	$-0.2^{\ +0.3}_{\ -0.3}$	269.7/270	$11.17 \pm 0.53^{\circ}$
P30	$15.4^{+1.2}_{-1.1}$	270.8/271	61.5 ± 6.5	0.5 ± 0.7	269.6/270	2.90 ± 0.30
P31	$12.4^{+0.9}_{-0.9}$	281.2/271	01.5 ± 0.5	0.5 ± 0.7	20).0/270	3.65 ± 0.34
P32	$10.3^{+0.9}_{-0.9}$	189.0/202	39.2 ± 5.0	-0.4 ± 0.6	181.7/201	1.58 ± 0.16
P33	$13.2^{+1.9}_{-1.7}$	263.4/202				3.37 ± 0.45
P34	$10.7^{+3.6}_{-3.4}$	230.6/272				0.43 ± 0.10
P35	$13.4^{+1.3}_{-1.2}$	342.4/339				2.32 ± 0.29
P36	$13.2^{+1.6}_{-1.4}$	326.7/340	53.6 ± 10.3	-0.3 ± 0.9	323.9/339	1.30 ± 0.18
P37	$11.7^{+1.4}_{-1.3}$	108.4/134			,	2.01 ± 0.32
P38	$12.6^{+1.2}_{-1.1}$	58.8/271	52.0 ± 6.3	0.1 ± 0.7	256.5/270	1.45 ± 0.17
P39	$11.3_b^{+2.5}$	94.1/134			,	0.16 ± 0.05
P40	$10.6^{+0.9}_{-0.9}$	186.7/204	41.2 ± 4.9	-0.04 ± 0.8	182.6/203	1.98 ± 0.23
P41	$9.2^{+2.4}_{-1.9}$	96.0/136			,	0.67 ± 0.18
P42 T_F	$12.2_{-1.1}^{+1.2}$	245.8/202	54.3 ± 8.9	-0.7 ± 0.5	237.9/201	2.20 ± 0.26
P43	$9.7^{+3.0}_{-2.7}$	84.8/135			·	0.53 ± 0.18
P44	$8.6_b^{+4.2}$	178.0/202				0.34 ± 0.11
P45	$8.5^{+2.2}_{-1.9}$	80.9/136				0.51 ± 0.15
P46	$12.5^{+3.0}_{-2.5}$	94.3/135				0.81 ± 0.27
P47	$12.0_{-2.4}^{+3.0}$	104.1/135				0.62 ± 0.18
P48	$7.8^{+2.0}_{-1.5}$	115.5/135				0.65 ± 0.17
P49	$9.5^{+1.9}_{-1.6}$	171.9/204	39.7 ± 8.9	-0.3 ± 1.3	170.4/203	0.42 ± 0.08
P50	$10.3^{+2.9}_{-3.8}$	142.0/204				0.63 ± 0.18
P51	$7.7^{+1.6}_{-1.6}$	184.8/273				0.30 ± 0.08
P52	$10.1^{+2.6}_{-2.3}$	120.6/135				0.26 ± 0.07
P53	$4.3_b^{+1.8}$	128.7/204				0.29 ± 0.10
P54	$11.1^{+3.6}_{-2.5}$	97.4/136				0.55 ± 0.17
P55	$11.3^{+2.3}_{-2.1}$	108.7/135				0.62 ± 0.17
P56	$4.4_b^{+6.0}$	159.0/204				0.24 ± 0.10

Table 4 (Continued)

	ВВ		COMPT			
ID	kT (keV)	C-Stat/DoF	E _{peak} (keV)	Index	C-Stat/DoF	Fluence ^a , ^b (10 ⁻⁸ erg cm ⁻²)
P57	$11.4^{+3.7}_{-2.9}$	127.8/204				0.18 ± 0.06
P58	$10.6^{+2.5}_{-2.2}$	231.6/272				0.45 ± 0.10

Notes. Bold entries represent the statistically preferred model. Uncertainties are 1σ .

^c Energy flux of COMPT model is used.

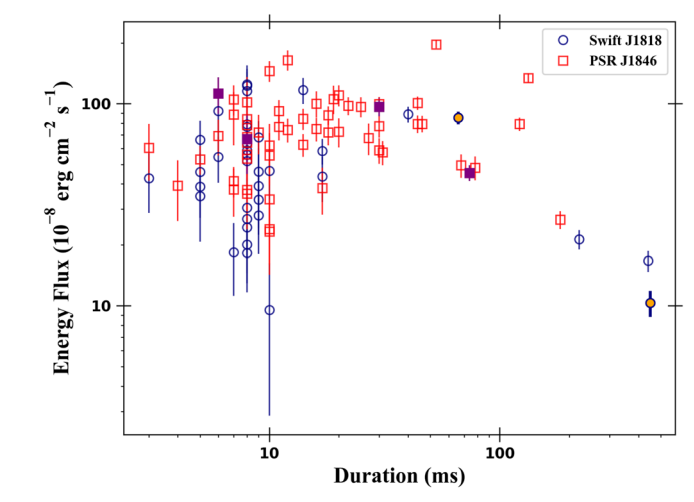


Figure 4. Scatter plot of burst duration and energy flux in the 8–200 keV of Swift J1818.0–1607 (blue circles) and PSR J1846.4–0258 (red squares) events. The events with filled symbols in orange and purple denote the triggered events of Swift J1818.0–1607 and PSR J1846.4–0258, respectively.

This plot could serve as a probe to understand the manner of burst energy injection in a magnetar source. For Swift J1818.0 –1607 (see the left panel of Figure 5), there is no major clustering of bursts in time (as is the case for PSR J1846.4–0258; Figure 5, right panel). It generally emitted isolated bursts on a timescale anywhere between one to seven days. Therefore, it exhibited an overall linear trend in cumulative fluence throughout its burst-active phase. The sudden increases in the cumulative fluence on days ~55 and 90 are caused by two events (S11 and S19, respectively) having longer duration (and hence higher fluence) relative to remaining events.

PSR J1846.4–0258, on the other hand, has characteristically different cumulative burst fluence behavior. The burst-active phase starts on 2020 July 10 and progresses with repeated bursts once every 3–4 days, yielding a linear trend comparable to that of Swift J1818.0–1607 in cumulative burst fluence. Then, on July 18, the source exhibits its most active behavior, emitting 32 bursts, therefore, showing a very rapid rise in cumulative fluence about 12 days after the outburst onset. Then, the burst emission of PSR J1846.4–0258 abruptly slowed down by exhibiting bursts once every 2–7 days with relatively low fluence. Its cumulative burst fluence follow again a linear trend similar to the beginning, after the 12th day; therefore, the cumulative fluence evolution forms a knee on the 12th day after the onset.

To quantify the trend, we fit the cumulative fluence in time segments of characteristically different trends with a linear function for each source. The fit intervals for Swift J1818.0 -1607 were between the days $0-52,\,53-82,$ and 88-145. We find the cumulative fluence increase rates of $(1.4\pm0.1)\times10^{-14},\,(0.7\pm0.5)\times10^{-14},\,$ and $(1.5\pm0.2)\times10^{-14}$ erg cm $^{-2}$ s $^{-1}$, respectively. For PSR J1846.4–0258, we selected events within 0–8, 8–10, and 11–81 days, and obtained slopes of $(1.7\pm0.5)\times10^{-14},\,(2070.7\pm18.6)\times10^{-14},\,$ and $(2.0\pm0.3)\times10^{-14}$ erg cm $^{-2}$ s $^{-1}$, respectively.

Palmer (1999) analyzed cumulative energy (count) trends using 134 bursts detected from SGR 1806–20. From the linear trends in time, they concluded that some bursts from the prolific magnetar act like relaxation systems; namely, they argue that some active sites on the neutron star accumulate energy, which is released suddenly but usually in an incomplete manner. Our results for Swift J1818.0–1607 resemble the cumulative trends of SGR 1806–20 (left panel of Figure 5), as well as in the first 12 days and after the 15th day of the activity of PSR J1846.4–0258 (right panel of Figure 5).

All events from both Swift J1818.0-1607 and PSR J1846.4 -0258 are adequately described with a single BB function. The BB temperature on average is slightly lower for Swift J1818.0 -1607 than PSR J1846.4-0258 (weighted averages 7.83 ± 0.25 keV versus 11.14 ± 0.15 keV). Having a singlecomponent thermal spectrum is usually not the case for bursts from prolific magnetars, as their spectra require more complex and usually broader spectral shapes, often described with the COMPT model or the BB+BB function, implying simultaneous emission from at least two distinct sites at different temperatures (Israel et al. 2008; Lin et al. 2012). However, one of the most prolific and radio-emitting magnetars, SGR J1550 -5418 exhibited two active episodes in 2008 October and 2009 March-April, during which bursts detected were successfully described with a single BB form (von Kienlin et al. 2012). The average blackbody temperature of the bursts in the former active epoch was $11.9 \pm 0.1 \, \text{keV}$ and that of bursts detected in the latter epoch was $8.9 \pm 0.1 \, \text{keV}$ (von Kienlin et al. 2012). The most active burst phase of SGR J1550-5418 was in 2009 January-February, and burst spectra during that era were complex. Based on the spectral parameters, we conclude that collective spectral behavior of bursts from Swift J1818.0-1607 resembles that of SGR J1550-5418 events in 2009 March-April, while collective spectral properties of PSR J1846.4-0258 bursts are similar to that in the 2008 October episode of this prolific magnetar.

T_F Bursts triggered GBM.

TS Bursts triggered Swift/BAT.

^a Calculated in 8-200 keV.

^b Negative error cannot be determined.

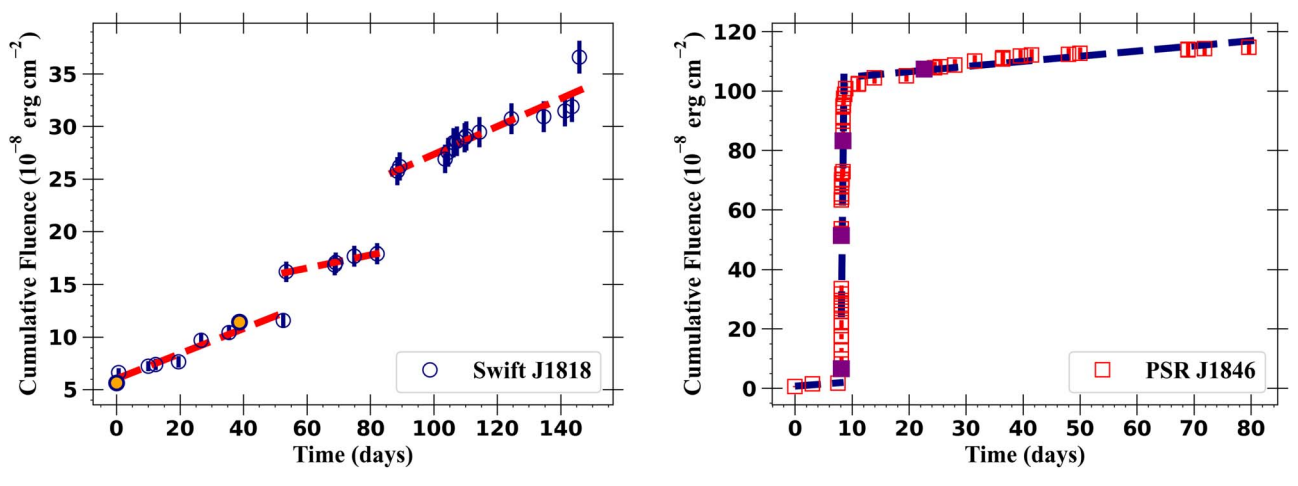


Figure 5. Time evolution of cumulative burst fluence for Swift J1818.0–1607 (left) and PSR J1846.4–0258 (right) since 2020 February 3 and 2020 July 10, respectively. The reference time is the time of first burst observed for each source (see the Table 1 and 2). The filled points represent the triggered events. The dashed lines are the best-fit linear trends.

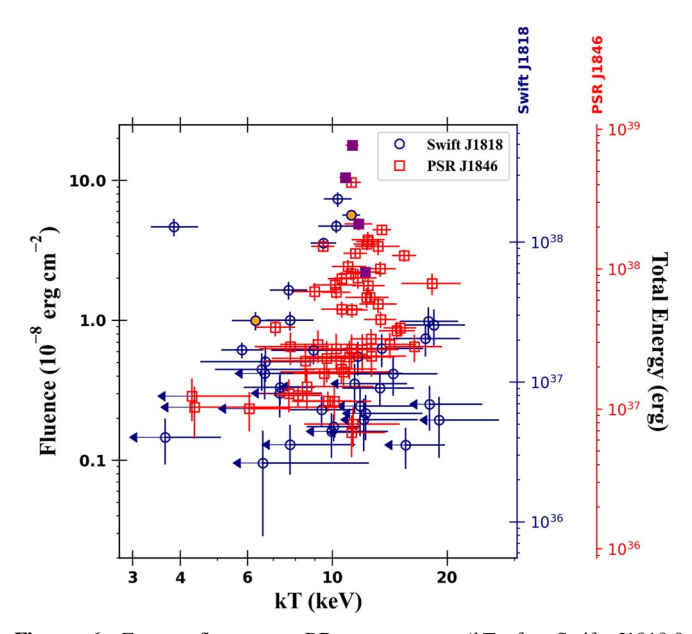


Figure 6. Energy fluence vs. BB temperature (kT) for Swift J1818.0 -1607 bursts (blue circles) and PSR J1846.4-0258 bursts (red squares). The corresponding burst energy scales for Swift J1818.0-1607 and PSR J1846.4 -0258 are displayed on the right vertical axis.

To address the overall burst energetics, we have also investigated whether the energy fluence, that is, time-integrated energy flux, of bursts is correlated with the BB temperature (kT)of the event. For individual bursts, fluence implicitly scales with the temperature, as well as the size of BB emitting area and the duration of the burst. We present the scatter plots of energy fluence versus kT for Swift J1818.0-1607 and PSR J1846.4–0258 in Figure 6. We find no significant correlation between fluence and kT for both Swift J1818.0-1607 bursts (Spearman's rank order correlation coefficient, $\rho = -0.07$ and probability of occurrence by random data set, P = 0.71) and for PSR J1846.4-0258 bursts ($\rho = 0.45$, P = 0.0005). We also calculated the energy content of each burst from both sources and indicate their energetics on the right labels of Figure 6. Here, we assumed the distances to Swift J1818.0-1607 and PSR J1846.4-0258 as 4.8 and 6.0 kpc, respectively. We find that, on average, the bursts of PSR J1846.4-0258 are more

energetic than those of Swift J1818.0–1607: The weighted average of the inferred total energy of Swift J1818.0 -1607 bursts is $8.0 \pm 0.6 \times 10^{36}$ erg and that of PSR J1846.4 -0258 bursts is $1.5 \pm 0.1 \times 10^{37}$ erg.

The single blackbody fits for these bursts indicate that their emission regions do not exhibit a range of temperatures that would be typical of enlarged volumes that permit adiabatic cooling or heating of the radiating plasma. If these regions are comparable to or considerably larger than the stellar radius, then magnetic field curvature/flaring would allow adiabatic expansion or compression of the gas along flux tubes. The temperature changes associated with these gas motions would lead to broader spectra akin to those that are seen in the 2008-2009 active burst phase of SGR J1550-5418 (Lin et al. 2012), and also the peculiar hard X-ray burst (Younes et al. 2021) that accompanied the fast radio burst detected from SGR J1935+2154 in 2020 April. Thus, the general narrowness of the burst spectra constrains the emission zones to being quite compact, and from Figure 7 below, we infer that the emission regions are in the range of \sim 0.7–5.0 km. These are smaller than the stellar radius, and so one does not anticipate significant adiabatic evolution of the gas temperature. Note that this compactness inference can apply to both crustal rupture (e.g., Thompson & Duncan 1995; Gourgouliatos & Lander 2021) and magnetospheric magnetic reconnection (e.g., Lyutikov 2003) activation scenarios. If these narrow spectrum bursts are less energetic than their broader counterparts from active phases of radio-emitting magnetars, then this spectral signature may be a key property that distinguishes high-field rotationpowered pulsars from their magnetar cousins.

We computed the circular area of the blackbody emitting region for each burst from Swift J1818.0–1607 and PSR J1846.4–0258 given the BB temperatures and distance to the sources. In Figure 7, we present the calculated BB emitting area (R^2) as a function of kT. We find that bursts from both sources roughly follow the Stefan–Boltzmann law for an isotropic radiation field (that is, $R^2 \propto kT^{-4}$) but with slight deviations. For Swift J1818.0–1607, the area ranges from 0.05 to 40 km² following the power-law trend with an index of -3.31 ± 0.35 . For PSR J1846.4–0258, the range of burst emitting areas is nearly the same, extending from 0.2 to 40 km², following the power-law function with an index of -3.38 ± 0.34 . As seen in Figure 7, the average luminosity of all bursts in our sample are of the order of

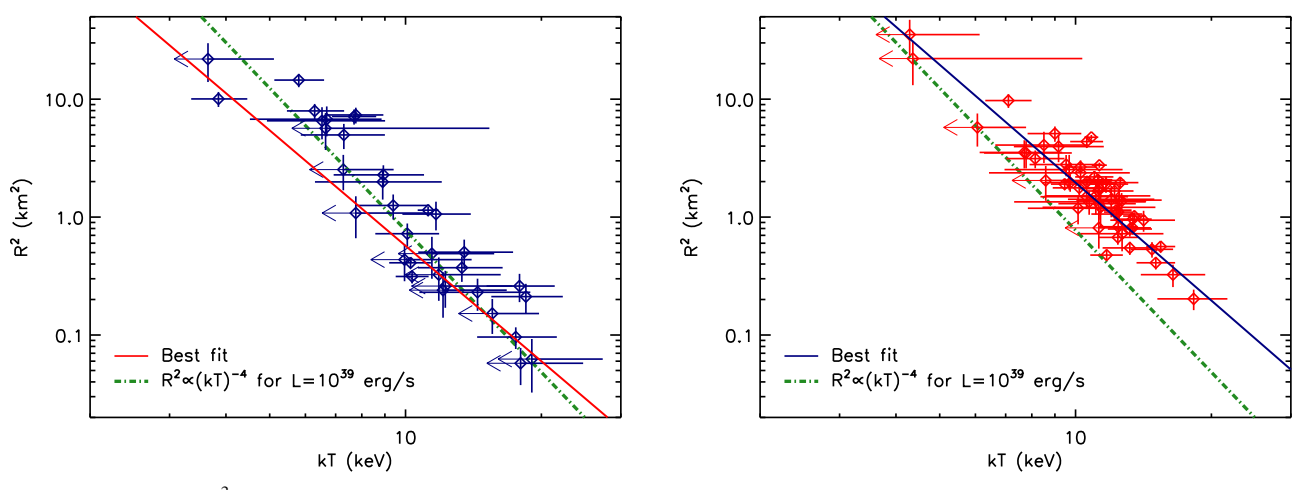


Figure 7. BB emitting area (R^2) vs. kT for Swift J1818.0–1607 bursts (left) and PSR J1846.4–0258 bursts (right). The best-fit lines are shown as solid lines. $R^2 \propto (kT)^{-4}$ is shown as a green dashed–dotted line, which corresponds to the luminosity of $L=10^{39}$ erg s⁻¹. The arrows indicate that the lower uncertainties of the kT values cannot be constrained.

10³⁹ erg s⁻¹, which is on the lower end of typical SGR bursts. We find that the luminosity of Swift J1818.0–1607 bursts are lower than that of PSR J1846.4–0258 bursts on average, as also indicated in Figure 6.

The observed correlation in Figure 7 with the associated power-law indices indicate a modest departure from the Stefan-Boltzmann law, $\Omega R^2 T^4 = \text{constant}$. As stated above, this relation in Figure 7 is invoked for an isotropic burst emission with a solid angle $\Omega = 4\pi$, a common practice in a wide variety of astrophysical settings. The observed correlations are somewhat weaker in temperature, indicating that $\Omega \propto T^{-\alpha}$, for $\alpha \sim 0.6$ –0.7, so that the radiation is not isotropic, and greater anisotropy (i.e., reduced solid angle) occurs at high temperatures. The strong magnetic fields of burst environs in magnetar magnetospheres guarantee anisotropy of the radiation emerging from optically thick burst emission zones. Results from the polarized radiation transport study of neutron star atmospheres by Barchas et al. (2021) can be applied to magnetospheric bursts, which most likely emanate from magnetic flux tubes or surfaces that are bounded by field lines. Thus the burst emission region is analogous to atmospheric equatorial locales, where the B field lies tangential to the outer surface.

Inspection of Figure 5 of Barchas et al. (2021) reveals significant anisotropies below and near the cyclotron frequency $\omega_{\rm B}$, with the level of anisotropy declining as the photon frequency $\omega \ll \omega_{\rm B}$ gets lower; there is a moderate residual decrement of intensity near the surface "horizon." Since the \sim 10 keV X-ray temperatures of the Fermi-GBM bursts studied here are most likely below the cyclotron frequency in the magnetospheric fields, the lower the temperature, the more isotropic the radiation should be. Accordingly, positive exponents α should emerge in the $\Omega \propto T^{-\alpha}$ inference, and this is exactly what is apparent in Figure 7. The fact that α is not small implies that the mean photon energy of ~ 30 keV is a sizable fraction of the cyclotron energy i.e., $\hbar\omega_{\rm B}\sim 50{\text -}500~{\rm keV}$, so that one can deduce that in the burst regions, the field is typically in the range of $\sim 5 \times 10^{12}$ –5 $\times 10^{13}$ G, values that are realized in the inner magnetosphere not too remote from the stellar surface. The actual value of α will be influenced by a convolution of different viewing perspectives relative to curved magnetic flux surfaces sampled by the entire burst ensemble.

Finally, we also find no obvious spectral evolution in bursts of Swift J1818.0–1607 and PSR J1846.4–0258, as seen in

SGR J1550-5418 (von Kienlin et al. 2012) and SGR J1935 +2154 (Lin et al. 2020a) even though the burst-active episodes of the two sources studied here are sufficiently long, spanning a few months to a year. All of these differences we find in our study between the bursts of these radio-emitting, high-B neutron stars and those of prolific magnetars may point to observable properties that distinguish the two classes of high-B sources.

We thank the reviewer for constructive comments that helped improve the clarity of the manuscript. M.U., Ö.K., Y.K., and C.G. acknowledge the support from the Scientific and Technological Research Council of Turkey (TÜBÍTAK grant No. 118F344). M.G.B. acknowledges the generous support of the National Science Foundation through grant AST-1813649.

Appendix A SGR Burst Search & Classification Methodologies

Here we describe the methodologies we employed for identifying potential SGR bursts within the GBM data. The onboard triggering algorithm of GBM detectors is based on signal-to-noise ratio, $S/N = (R_S - R_B)/\sigma$, where R_S is the source count rate, R_B is the background count rate, and $\sigma = \sqrt{N_B}/t$, where N_B is the total background counts and t is the duration (or time resolution) of the data bin. The GBM triggering threshold varied from 4.5 σ to 8 σ in four possible energy bands, 25–50, 50–300, >100, or >300 keV (von Kienlin et al. 2020). To identify a trigger of interest, two or more detectors need to simultaneously record count rates exceeding the threshold, to exclude possible triggers due to non-astrophysical sources.

For our burst search used in this study, we used the CTTE data of 12 GBM Na I detectors binned to 8 ms over an energy range of 10–100 keV. These particular time resolution and the energy range were chosen to optimize the search for finding SGR bursts. We employed the three statistical methods described below to look for a significant increase in the count rates in each Na I detector separately.

A.1. The Search Methods

The three search methods we employed are as follows:

1. Bayesian Statistics—The Bayesian statistics search method first represents the binned lightcurve with a series of

step functions, ("Bayesian blocks") based on the change points determined by Bayesian statistics (Scargle et al. 2013), which can be of different widths (duration) and heights (intensity). Since we are searching for short SGR events, the blocks >1 s before and after each Bayesian block were considered as the background blocks, from which the average background rates were calculated. Subsequently, the blocks <1 s with the count rates above the average background rates found in two or more detectors were considered as an event candidate.

2. Poisson Statistics—With the Poisson statistics search method, for each data segment with a certain number of time bins, the number of counts in the *i*th time bin was compared to a local mean λ_i . The local mean was calculated from a 10 s stretch of data before and after the time bin being evaluated. We left out a time window of 3 s immediately before and after the bin under evaluation so that it would not contribute to the local mean. For the comparison, we used Poisson statistics and determined the probability of the number of counts in a time bin (n_i) greater than the local mean (λ_i) occurring by chance as follows:

$$P_i(t_i) = \frac{\lambda_i^{n_i} e^{-\lambda_i}}{n_i!}$$

The chance probability $\leq 10^{-4}$ in two or more detectors were considered as a candidate event. The threshold was chosen since our pre-search comparison study showed that $P \sim 10^{-4}$ corresponds to a S/N of 4.5σ , which is the lowest threshold we use for the S/N search method as well as in the GBM on-board trigger algorithm. Below this threshold, we found that false positive detection becomes much more frequent.

3. Signal-to-Noise Ratio (S/N)—This method is essentially the same approach as the GBM trigger algorithm with the lowest S/N but we used a unique energy range (10–100 keV) aimed at catching SGR bursts. The background rates were calculated in the same manner as the Poisson method described above, and the S/N = $(R_S - R_B)/(\sqrt{N_B}/t)$ was calculated for each of the time bins. Bins with S/N \geqslant 4.5 σ in two or more detectors are considered as a candidate event.

We note that for both Poisson and S/N methods, when the candidate events were identified in a consecutive time bins, they were considered as a single event, with the default duration of $8 \text{ ms} \times$ the total number of consecutive bins. Since this default duration was calculated for each detector separately, this may vary from detector to detector.

A.2. Event Filtering and Classification

The candidate events found with any of the above methods include false detection caused by the spacecraft's passage through the South Atlantic Anomaly (SAA) region, as well as the events due to known sources such as solar flares, ¹⁴ active X-ray pulsars, ¹⁵ or Fermi-GBM triggers that are identified as non-SGRs in the Fermi-GBM Trigger Catalog ¹⁶ Since the exact times of these events are known, we first filtered these events out of our sample. We also filtered out the events that were previously identified as the bursts from other SGRs in literature and in other on-going investigations within our team. The remaining candidate events were subjected to an event-

classification algorithm with a Bayesian probability approach, similar to the method used for the on-board classification of GBM triggers (Briggs et al. 2007). Over 100 on-board trigger algorithms are used with GBM, each with a particular energy range, timescale, and threshold (von Kienlin et al. 2020). When GBM is triggered, the triggered event is immediately classified by calculating the probabilities of the event being a GRB, SGR, solar flare, Terrestrial Gamma Flash (TGF), X-ray transient, or a particle event, based on the observed parameters such as the event's rough location, hardness ratio, count ratio, and the spacecraft's geomagnetic coordinates.

Here in our classification algorithm, we used the candidate event's duration and other observed parameters except the event location. We first calculated the duration and the hardness ratio of each of the candidate events using the combined lightcurve of the brightest (i.e., most significant detection) two detectors with 1 ms time resolution and generated the Bayesian block representation of the combined lightcurve in 10–100 keV. The blocks <4 s with count rates exceeding the average count rates of the background blocks (≥4 s) were taken as the event blocks (= duration). We then calculated the hardness ratio for each candidate in the energy range of 10–1000 keV, with three energy "pivot" points (E_{piv}): 25, 50, and 75 keV. The hardness ratio was defined as the ratio of background-subtracted counts in E_{piv}-1000 keV over 10 keV- $E_{\rm piv}$, at the event start time. These $E_{\rm piv}$ values were chosen since we found these hardness ratios to best distinguish SGR bursts from short GRBs and TGFs that have similar duration based on the triggered event properties. Here, we use the same background levels calculated for the duration.

To determine the prior for our Bayesian probability classification algorithm, we utilized the statistics and properties of over 8000 GBM-triggered events. Our event search was done with 8 ms time resolution over an energy range of $10-100 \, \text{keV}$; therefore, we listed the events that were triggered by the algorithms similar to ours in time and energy, and determined the number of triggered events in various event classes. This was taken as the prior for calculating the likelihood, and we determined the posterior probability for the candidate belonging to a specific event class based on the duration and hardness ratio values. All events with the posterior probability >90% for the SGR class were kept in our sample.

ORCID iDs

Mete Uzuner https://orcid.org/0000-0002-4387-7684
Özge Keskin https://orcid.org/0000-0001-9711-4343
Yuki Kaneko https://orcid.org/0000-0002-1861-5703
Ersin Göğüş https://orcid.org/0000-0002-5274-6790
Oliver J. Roberts https://orcid.org/0000-0002-7150-9061
Lin Lin https://orcid.org/0000-0002-0633-5325
Matthew G. Baring https://orcid.org/0000-0003-4433-1365
Can Güngör https://orcid.org/0000-0003-3791-3754
Chryssa Kouveliotou https://orcid.org/0000-0003-1443-593X
Alexander J. van der Horst https://orcid.org/0000-0001-9149-6707

References

Ambrosi, E., Barthelmy, S. D., D'Elia, V., et al. 2020, GCN, 27672, 1 Barchas, J. A., Hu, K., & Baring, M. G. 2021, MNRAS, 500, 5369 Barthelmy, S. D., Gropp, J. D., Kennea, J. A., et al. 2020, GCN, 27696, 1 Bernardini, M. G., D'Avanzo, P., Klingler, N. J., et al. 2020, GCN, 28055, 1

George Younes https://orcid.org/0000-0002-7991-028X

https://hesperia.gsfc.nasa.gov/fermi_solar

¹⁵ https://gamma-ray.nsstc.nasa.gov/gbm/science/pulsars.html

https://heasarc.gsfc.nasa.gov/FTP/fermi/data/tdat/heasarc-fermigtrig.tdat.

```
Blumer, H., Safi-Harb, S., McLaughlin, M. A., & Fiore, W. 2021, ApJL, 911, L6
Bochenek, C. D., Ravi, V., Belov, K. V., et al. 2020, Natur, 587, 59
Briggs, M. S., Connaughton, V., Paciesas, W., et al. 2007, in AIP Conf. Ser.
   921, The First GLAST Symposium, ed. S. Ritz, P. Michelson, &
   C. A. Meegan (Melville, NY: AIP), 450
Champion, D., Cognard, I., Cruces, M., et al. 2020, MNRAS, 498, 6044
CHIME/FRB Collaboration, Andersen, B. C., Bandura, K. M., et al. 2020,
    Natur, 587, 54
Duncan, R. C., & Thompson, C. 1992, ApJL, 392, L9
Esposito, P., Rea, N., Borghese, A., et al. 2020, ApJL, 896, L30
Evans, P. A., Gropp, J. D., Kennea, J. A., et al. 2020a, GCN, 27373, 1
Evans, P., Gropp, J. D., & Kennea, J. A. 2020b, GCN, 27373, 1
Gavriil, F. P., Gonzalez, M. E., Gotthelf, E. V., et al. 2008, Sci, 319, 1802
Goldstein, A., Hamburg, R., Wood, J., et al. 2019, arXiv:1903.12597
Gotthelf, E. V., Safi-Harb, S., Straal, S. M., & Gelfand, J. D. 2021, ApJ,
   908, 212
Gotthelf, E. V., Vasisht, G., Boylan-Kolchin, M., & Torii, K. 2000, ApJL,
   542, L37
Gogus, E., Lin, L., Kaneko, Y., et al. 2016, ApJL, 829, L25
Gourgouliatos, K. N., & Lander, S. K. 2021, MNRAS, 506, 3578
Gogus, E., Woods, P. M., Kouveliotou, C., et al. 1999, ApJL, 526, L93
Gogus, E., Woods, P. M., Kouveliotou, C., et al. 2000, ApJL, 532, L121
Gronwall, C., Gropp, J. D., Kennea, J. A., et al. 2020, GCN, 27746, 1
Hu, C. P., Begicarslan, B., Guver, T., et al. 2020, ApJ, 902, 1
Israel, G. L., Romano, P., Mangano, V., et al. 2008, ApJ, 685, 1114
Karuppusamy, R., Desvignes, G., Kramer, M., et al. 2020, ATel, 13553, 1
Kaspi, V. M., & Beloborodov, A. M. 2017, ARA&A, 55, 261
Kocevski, D., Burns, E., Goldstein, A., et al. 2018, ApJ, 862, 152
Kouveliotou, C., Dieters, S., Strohmayer, T., et al. 1998, Natur, 393, 235
```

Krimm, H. A., Lien, A. Y., Page, K. L., et al. 2020, GCN, 28187, 1

```
Kuiper, L., Harding, A. K., Enoto, T., et al. 2020, ATel, 13985, 1
Leahy, D. A., & Tian, W. W. 2008, A&A, 480, L25
Liddle, A. R. 2007, MNRAS, 377, L74
Lin, L., Göğüş, E., Roberts, O. J., et al. 2020a, ApJL, 902, L43
Lin, L., Göğüş, E., Roberts, O. J., et al. 2020b, ApJ, 893, 156
Lin, L., Gogus, E., Baring, M. G., et al. 2012, ApJ, 756, 54
Lower, M. E., Shannon, R. M., Johnston, S., & Bailes, M. 2020, ApJL,
   896, L37
Lyutikov, M. 2003, MNRAS, 346, 540
Lyutikov, M. 2021, ApJ, 922, 166
Malacaria, C. & Fermi GBM Team 2020, GCN, 27674, 1
Meegan, C., Lichti, G., Bhat, P. N., et al. 2009, ApJ, 702, 791
Mereghetti, S., Savchenko, V., Ferrigno, C., et al. 2020, ApJL, 898, L29
Ng, C. Y., & Kaspi, V. M. 2011, in AIP Conf. Ser. 1379, AstroPhysics of
   Neutron Stars 2010: A Conference in Honor of M. Ali Alpar, ed. E. Göğüş,
   T. Belloni, & Ü Ertan (Melville, NY: AIP), 60
Olausen, S. A., & Kaspi, V. M. 2014, ApJS, 212, 6
Palmer, D. M. 1999, ApJL, 512, L113
Petroff, E., Hessels, J. W. T., & Lorimer, D. R. 2019, A&ARv, 27, 4
Petroff, E., Hessels, J. W. T., & Lorimer, D. R. 2022, A&ARv, 30, 2
Rajwade, K. M., Stappers, B. W., Lyne, A. G., et al. 2022, MNRAS, 512, 1687
Scargle, J. D., Norris, J. P., Jackson, B., & Chiang, J. 2013, ApJ, 764, 167
Thompson, C., & Duncan, R. C. 1995, MNRAS, 275, 255
Thompson, C., & Duncan, R. C. 1996, ApJ, 473, 322
van der Horst, A. J., Kouveliotou, C., Gorgone, N. M., et al. 2012, ApJ,
   749, 122
von Kienlin, A., Gruber, D., Kouveliotou, C., et al. 2012, ApJ, 755, 150
von Kienlin, A., Meegan, C. A., Paciesas, W. S., et al. 2020, ApJ, 893, 46
Younes, G., Kouveliotou, C., van der Horst, A. J., et al. 2014, ApJ, 785, 52
Younes, G., Baring, M. G., Kouveliotou, C., et al. 2021, NatAs, 5, 408
```